Experimental investigation of the rotational characteristics of a novel hybrid laminated glass beam-column connection prototype.

Mirko Pejatović [a], Sébastien Moerman [a], Robby Caspeele [a], Jan Belis [a]

[a] Ghent University, Department of Structural Engineering and Building Materials, Ghent, Belgium

corresponding author's mail: mirko.pejatovic@ugent.be

ABSTRACT

This article presents an experimental investigation of the rotational characteristics of a novel hybrid laminated glass beam-column connection prototype. The testing of small-scale prototype specimens is conducted to assess the effect of the main structural parameters such as glass pane thickness, interlayer and reinforcement properties on the rotational characteristics. To explore the possibility of using different lamination technologies for the realization of the joints, two different bonding technologies are considered separately: (a) autoclave and (b) UV-curing lamination. The specimens are subjected to a pair of self-equilibrated compressive forces up to failure in a custom-made setup. Digital image correlation (DIC) measurements together with strain gauges are used for tracking the kinematics of the main components.

It was found that the prototype is able to develop a significant post-fracture and rotational capacity in a properly balanced combination of structural and material parameters. The results are presented in terms of moment-rotation (M - θ) curves, strains evolution in the steel and evolution of the crack patterns. Experimental observations suggest that depending on the choice of structural parameters three failure modes are possible: (a) crushing failure of the joint core, (b) plastic failure of the adjoining sections and (c) failure due to debonding of one of the bars in tension. It is concluded that one can achieve a desirable post-fracture and ultimate behaviour by properly balancing the structural and material parameters. Additionally, pull-out opening and tensile stresses in steel are measured at the interrupted section, revealing a transition in sectional behaviour from fully interrupted to a hybrid section over a certain transition length.

KEYWORDS

Laminated glass, Moment-resisting frames, Beam-to-column connections, Beam, Column, Structural safety

NOMENCLATURE

Latin characters: lower case

h	height of the hybrid section
a	testing length of the legs
t_i	thickness of the inner glass panes
t_e	thickness of the outer glass panes
$t_{int.}$	thickness of the adhesive interlayer
b_s	width of the reinforcement steel bar
h_s	height of the reinforcement steel bars
ρ_s	geometrical reinforcement ratios
f_y	yield stress

f_t	tensile strength
w	pull-out displacement
r	local axis

Latin characters: upper case

A_s	tensile reinforcement area
E_s	modulus of elasticity of steel
A_g	cross-sectional area of glass
M	bending moment at the adjoining section
M_f	bending moment at the adjoining section at the first fracture
M_u	bending moment at the adjoining section at failure
T_s	pull-out force
F_u	ultimate force

Greek characters: lower case

ρ_s	geometrical reinforcement ratios
ρ	density
ν	Poisson coefficient
θ	relative rotation
θ_b	rotation of the beam
θ_c	rotation of the column
θ_f	relative rotation at the first fracture
θ_u	relative rotation at failure
ε_s	strain in a steel bar
ε_y	yielding strain
ε_t	ultimate tensile strain
$\varepsilon_{sg1,f}$	tensile strain in a steel bar on the side of the glass interruption at the first fracture
$\varepsilon_{sg2,f}$	tensile strain in a steel bar on the side of the uninterrupted glass at the first fracture
$\varepsilon_{sg1,u}$	tensile strain in a steel bar on the side of the glass interruption at failure
$\varepsilon_{sg2,u}$	tensile strain in a steel bar on the side of the uninterrupted glass at failure
$\sigma_{s,hyb.}$	tensile stress in the outer fibres of the reinforcement in a hybrid section
$\sigma_{s,inter.}$	tensile stress in the outer fibres of the reinforcement in an interrupted section

Abbreviations

CF	crushing failure
PF	plastic failure
DF	debonding failure
SG	SentryGlas®
UV	UVEKOL®

1. INTRODUCTION

Glass, being a brittle material, lacks the ability to redistribute stresses beyond its strength and is susceptible to an unsafe form of failure [1]. Hybrid glass members have been developed with different structural concepts related to the type and bonding of the reinforcement [2]–[4]. Properly bonded reinforcement enables a component to develop post-fracture capacity under accidental load events. However, additional safety resources such as stress redistribution and system action may be needed to assure an adequate safety level of the system [5]. The appearance of a crack in laminated glass is typically succeeded by the localized debonding of the interlayer from a glass surface and substantial plastic deformations [6] When subjected to shear loading, as is the case for laminated glass beams, adhesive interlayers like SentryGlas® (SG) offer additional tensile resistance [7]. Some relevant structural safety aspects of a reinforced glass frame are illustrated in Fig. 1.

The behaviour of connections plays a crucial role in determining the overall performance of the system. General trends in the development of adhesive and mechanical connections in transparent structures are presented in [8]. Mechanical glass connections refer to a method of joining glass elements in structures using e.g. bolts. While these connections are commonly employed and can offer strength and stability, there have the inherent risks of breakage associated with them. The research in recent years aims to develop innovative adhesive connection methods as alternatives to traditional bolted connections [9], [10].

Substantial enhancements to both the load-bearing capacity and the aesthetics of structural glass connections have been achieved by a new type of adhesive connection, labelled as embedded laminated glass connections. Research on embedded connections and aspects of metal-glass bonding with different configurations ([11] [12], [13][14], [15][16]–[20][21]) indicates that these connections attain a relatively high load-bearing capacity. However, their mechanical response, including strength, stiffness and failure mode, is significantly influenced by both temperature and loading rate. The embedded connection concept is proven successful in practical, real-world projects (see e.g. [22], [23]).

One of the most relevant structural aspects of the behaviour of hybrid glass connections is the bond quality between the reinforcement and the glass. The structural properties of the bond between steel and glass (bonding area, interlayer stiffness and strength, durability, etc.) define the interaction between the two materials. Influence of temperature and humidity on the bond performance could be significant [24]. Findings from tests aimed at evaluating the strength of adhesive interlayers indicate that various factors, including the thickness of the adhesive layer, the impact of aging, the type of bonding surface, and dimensions, significantly influence the stiffness and resistance of the interlayer, both in shear and tension [25]–[27]. Additionally, pull-out tests were conducted to evaluate the bonding performance between reinforcement and glass, as well as shear and tensile tests for the glass-metal bond [24], [28]. It was observed that the pull-out behaviour is influenced by factors such as temperature, aging, and bond geometry.

To ensure a robust system performance, one has to make proper decisions while designing connections details, reinforcement continuity, lamination technology, etc. Sufficient knowledge about all of these aspects is necessary for the development of reliable design and analysis procedures. In particular, to build and study the behaviour of unbraced hybrid glass frames subjected to a combination of horizontal and vertical load, in-depth knowledge about rotational characteristics of the beam-column connection is required.

In case of moment-resistant beam-column joints, several solutions have been studied in the literature or implemented in existing projects [29]–[34]. However, the performance and safety of such connections have not been sufficiently quantified so far. The adequate knowledge in this field is not available yet and research activities such as those in this contribution are necessary.

In terms of robustness, well-designed hybrid glass-steel connections have to comply to the post-fracture structural performance of the system so that a desirable plastic collapse is achieved and eventual system actions (compressive and tensile membrane action) take place. The theory of plasticity suggests that a connection has to enable the development of the full plastic moment in one or more adjoining members. The development of a plastic hinge with a specific rotational capacity in a steel-reinforced glass member is eventually possible, provided that the reinforcement yields and the crushing of the glass in the compressed zone is prevented. This type of behaviour was observed in continuous beams tested by Martens et al [35]. These principles need to be ensured by a sufficient strength and rotational capacity of the joint provided by its constitutive components. Depending on structural typology and design parameters, joints subjected to in-plane bending may experience brittle failure [36]–[38]. In such cases, knowledge about the in-plane shear behaviour of the joint core is essential [39].

Contemporary architectural trends are moving towards a very high level of structural transparency, which typically can be realized using (structural) glass. To enable construction of large glass areas, one needs to overcome limitations in terms of dimensions, production, transportation, etc. For the practical realization of large-scale continuous glass systems, it is essential to have a modular system that is both structurally safe and transparent, with longitudinally connected glass beams. A novel approach to connecting beam components was developed in [40], with a primary emphasis on ensuring optimal structural safety at both the individual component and system levels. The approach enables enhancing transparency and maintaining a continuous visual appearance of the beams by using Cast-In-Place (CIP) bonding technology. This innovative concept can be extended to a two-dimensional framework (e.g. portal frames). In this case, robustness of frames could be attained through the application of a similar construction technique at location of e.g. beam-column joints [9]. CIP bonding technology allows on-site lamination, which is key for installing large laminated glass components in locations that are difficult or impossible to access with elements in one large piece. It also enables lamination with panel sizes that may significantly exceed the limits of standard production and/or transportation sizes. The benefits of this concept are the reason why research trends are taking a direction towards novel variants of cast-in-place connections [40]–[42].

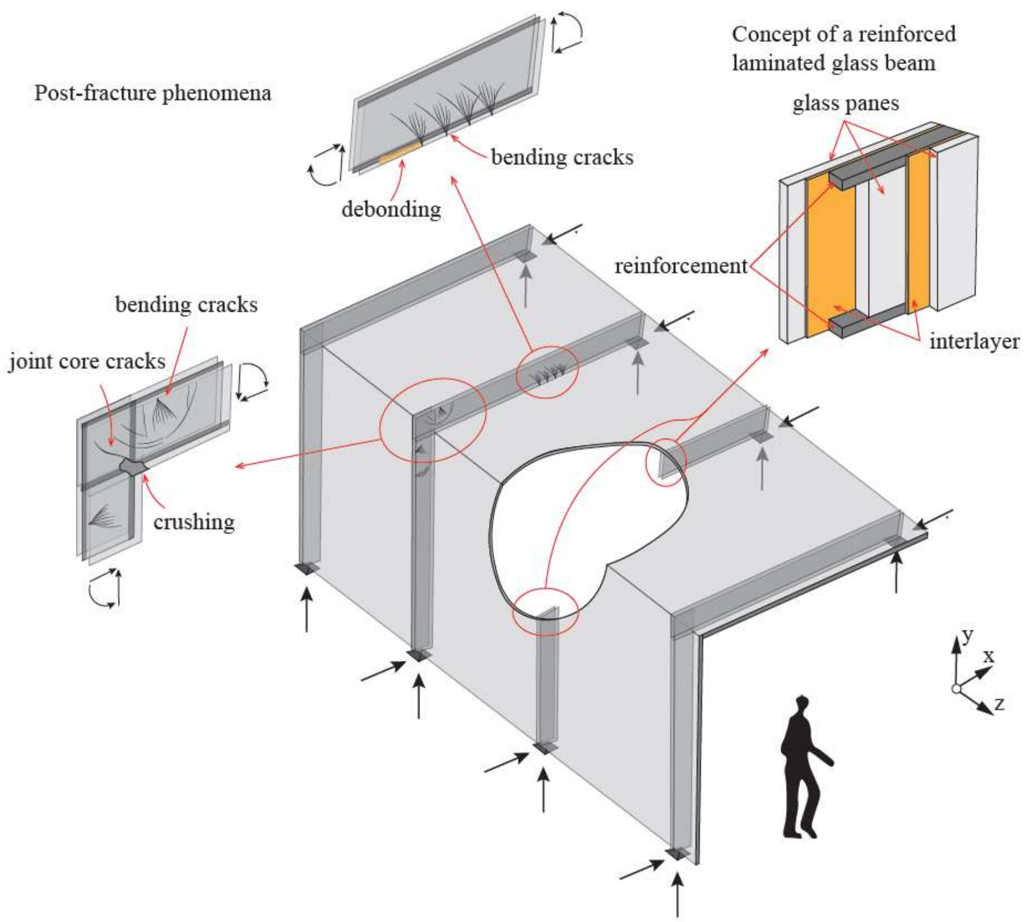

Fig. 1: Structural safety aspects in a reinforced glass structure.

This article presents an experimental investigation into the rotational characteristics of an innovative hybrid laminated glass beam-column connection prototype. The study explores the influence of glass pane thickness, interlayer properties and reinforcement characteristics on rotational behaviour. Two distinct lamination technologies: autoclave and UV-curing lamination, are separately considered for joint realization. The conclusion drawn is that a desirable post-fracture and ultimate behaviour can be realized by appropriately balancing structural parameters. Additionally, the pull-out opening and stresses in steel are measured at the interrupted section. It was observed that the sectional behaviour transits from a fully interrupted to a hybrid section over a certain transition length.

The modelling of steel-reinforced glass joints will be the subject of a future publication by the authors.

2. EXPERIMENTAL PROGRAM

2.1 Test specimens

Fig. 2 depicts the assembly of the connection prototype. It consists of a welded steel frame and triple-layered glass bonded together. The production of the connection starts with cutting of stainless steel bars. Subsequently, additional perforated anchorage plates are manufactured and all the steel components are welded together using tungsten inert gas (TIG) welding. This welding technique was chosen because it produces high-quality welds and can be used on a construction site. Welds are realized in a form of full tee and corner joints with single/double grooves. Welded sections have at least the strength provided by the original sections, so that the full plastic capacity of the bars could be exploited rather than a failure at the welds. To prevent local failure of glass and ensure proper steel-glass bonding, excessive welding material has to be removed and all the lateral steel surfaces need to be polished. Finally, all the components are assembled as illustrated in Fig. 2 and bonded by using two bonding techniques separately: autoclave and UV-curing lamination, which are explained in the subsequent sections.

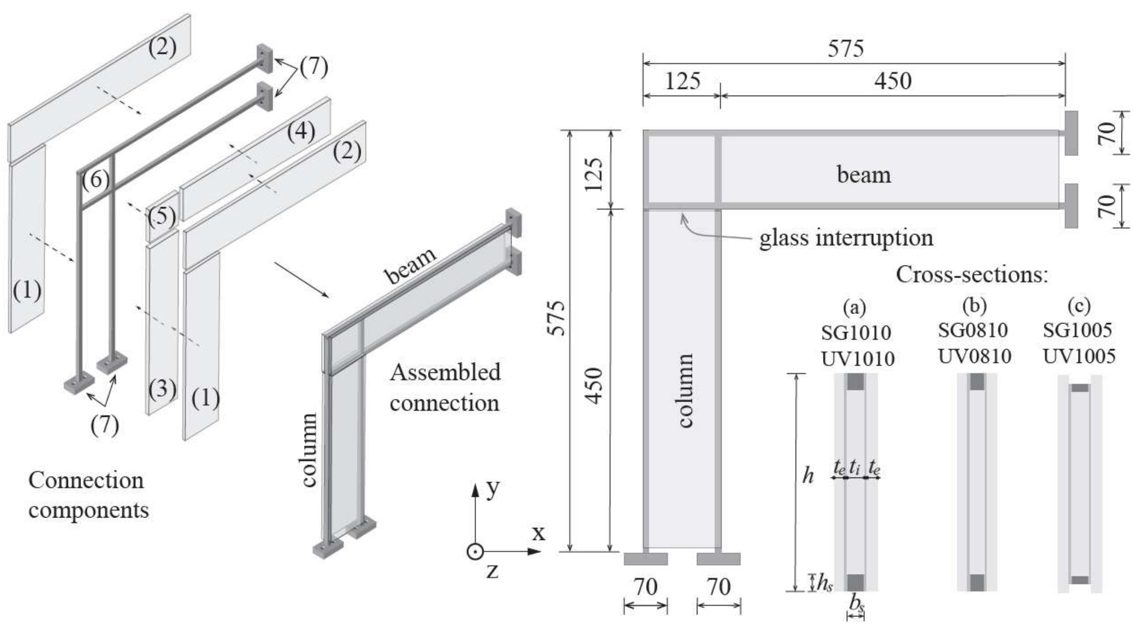

Fig. 2: Components of the connection prototype (dimensions in mm). The assembly consists of: (1) outer pane of the column, (2) outer pane of the beam, (3) inner pane of the column, (4) inner pane of the beam, (5) inner pane of the joint core, (6) welded reinforcement and (7) welded anchorage plates.

Fig. 2 also illustrates three geometrical configurations that are built in a small scale format. The initial configuration is denoted by (a) and its main features are described by the general designations in the same figure. Those are the height of the cross-section h, thickness of the interlayer $t_{int.}$, outer glass panes thickness t_e, inner glass panes thickness t_i, the width of the steel reinforcement bars b_s and the height of the steel reinforcement bars h_s. Additionally, the geometrical reinforcement ratio is given as $\rho_s = A_s / A_g$, where A_g is the area of glass in the cross-section. The configurations are designated by the type of interlayer used (SG for SentryGlas® and UV for UV-curable adhesive UVEKOL® S15), as well as the width (b_s) and height (h_s) of the steel reinforcement. For instance, 'SG1010' designates a specimen manufactured using SentryGlas® interlayer with steel reinforcement dimensions of b_s x h_s = 10 x 10 mm. The configurations (b) and (c) are built such that the inner pane glass thickness and the reinforcement ratio are reduced, respectively. Also, a lower steel quality is used for the last two configurations. Description and dimensions of the specimens are listed in Table 1. A series of trial tests were conducted with SG1010. However, only one specimen from SG1010 was tested correctly. For all other configurations, two tests were performed.

Table 1: Overview of the testing program: properties of all the configurations

Configuration	Number of tests	Interlayer	t_i [mm]	b_s [mm]	h_s [mm]	A_s [mm^2]
SG1010	1	SG	10	10	10	100
SG0810	2	SG	8	8	10	80
SG1005	2	SG	10	10	5	50
UV1010	2	UV	10	10	10	100
UV0810	2	UV	8	8	10	80
UV1005	2	UV	10	10	5	50

Note: for all the configurations h = 125 mm, $t_{int.}$ = 1.5 mm and t_e = 6 mm.

2.1.1 Material properties

Annealed float glass is used for all specimens in the joint test program. In the autoclave lamination procedure 1.52 mm thick SentryGlas® interlayer sheets are used [43]. In the UV-curing lamination procedure liquid resin UVEKOL® S15 is used [44]. The stainless steel rectangular bars are used as reinforcement. The stainless steel quality is EN 1.4301/1.4307 (AISI 304/304L). The reinforcement bars are tested in the uniaxial tensile tests. Fig. 3 summarizes stress-strain curves for all the bars. Yield stress is taken as an average value from the three tests at 0.2% plastic deformation. The elastic modulus of the steel is 180 GPa. This value is comparable to the one reported in the literature [45]. The yield stress and the elastic modulus of steel are taken as an average of three tests. The coefficient of variation for these two quantities is found to be less than 5%. The relevant mechanical properties of all the materials are presented in Table 2.

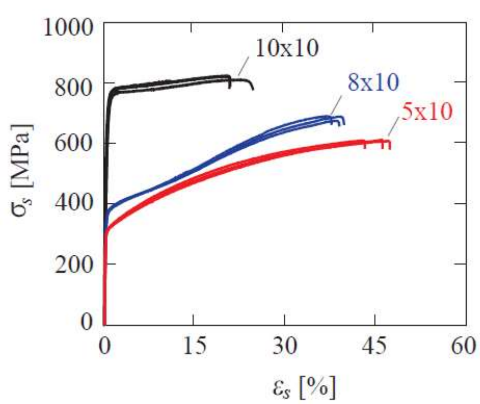

Fig. 3: Stress-strain diagram for the steel reinforcement.

Table 2: Mechanical properties of the materials based on the tensile tests and on literature [46][5][44][43].

Material	E	f_y	ε_y	f_t	ε_t
	[MPa]	[MPa]	[-]	[MPa]	[-]
Annealed float glass	70000	-	-	45	-
Stainless steel 10x10mm		670	0.0037	822	0.215
Stainless steel 8x10mm	180000	360	0.002	683	0.388
Stainless steel 5x10mm		310	0.0017	611	0.449
SentryGlas®	118.9	-	-	34.5	4.00
UVEKOL® S15	47.8	-	-	17.9	2.51

2.1.2 Autoclave lamination

In a standardized lamination procedure in the autoclave, components are bonded together using 1.52 mm thick SentryGlas® (SG) interlayer sheets. For the details of the lamination procedure, one can refer to [45].

2.1.3 UV-curing lamination

UV-curing lamination enables a hybrid glass-steel systems to be executed on a construction site. Fig. 4 illustrates the production process in the UV curing custom-made setup. The glass panes and the welded reinforcement are cleaned and degreased by means of isopropanol and positioned component-wise on a proper place. The positioning and fixing of all the components together and sealing of the gaps is done by means of transparent double-sided adhesive tape with a thickness of 1.5 mm (which is the envisaged thickness of the interlayer after the curing) and duct tape. The tapes are placed in a mindful manner so that the correct position and complete liquid tightness is ensured not impairing the bond surfaces. Such an assembly is placed on a reflective custom-made wooden table covered by aluminium foil.

The gaps are filled by dispensing resin with a standard plastic syringe. To fill the gaps, UV-curable liquid resin UVEKOL® S15 (UV) is employed. This is a one-component acrylic resin for bonding structural glass components [44]. It is applied in a 20 minutes curing process that does not require heating or pressure. The resin has been developed for security glazing with a set of favourable properties such as impact resistance, resistance to heat, UV light and humidity. This product was chosen for its transparency after curing, workability (easy injection into gaps), and good mechanical properties.

The curing is done continuously in a setup with a reflective table and by using UV lamps from both sides of the specimen (see Fig. 4(c)). The specimen is exposed to the radiation for at least 20 min with an intensity greater than or equal to 1 mW/cm^2 and an emission spectrum of 300 to 400 nm. Firstly, the column's gaps are filled and cured by means of vertically positioned UV lamps, which are illustrated in Fig. 4(a). Upon finishing the curing of the column, the beam and the joint core are cured in a similar manner by the lamps positioned horizontally (see Fig. 4(b)). For the purpose of scale, the 0.5m legend is included in the same figure.

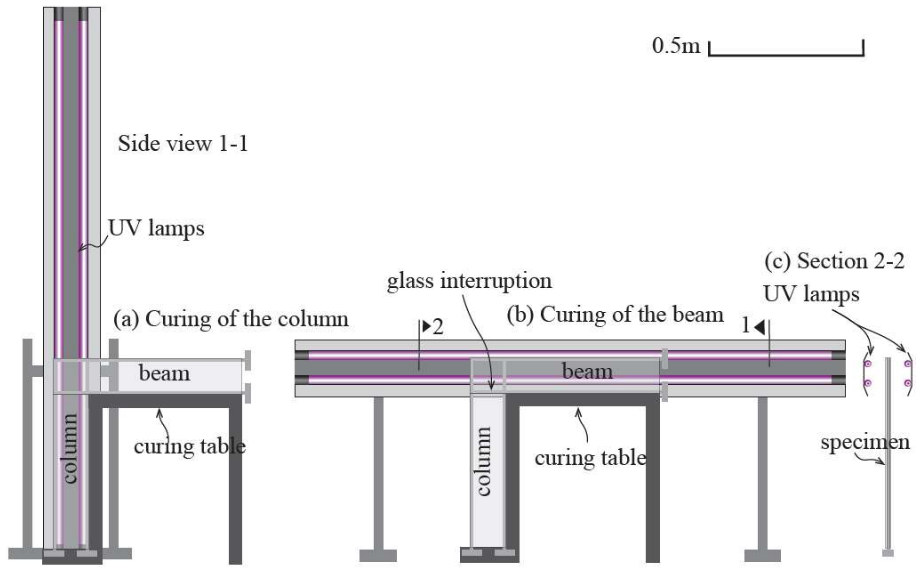

Fig. 4: Side view of the curing setup with a reflective table and UV lamps. (a) Curing of the column, (b) curing of the beam and (c) section of the setup in case of a beam curing.

2.2 Test setup and test procedure

A customized test setup was built to reproduce a realistic state of stresses in the connection, as depicted in Fig. 5(a). A common arrangement of setup elements for testing L-shaped joints is used. A similar arrangement is used for a corner joint in the two-sided bonded glass-steel façade unit [47]. The setup consists of an L-shaped specimen inclined at 45°, a testing machine, a steel socket, a steel attachment with a pin, and lateral restraints. A graphical representation of the socket is provided in Fig. 5(c). The steel socket is constructed using perforated steel plates connected by bolts. It serves to secure the specimen from above to the movable part of the machine and from the bottom to the fixed part. Measures are taken to prevent direct contact between the steel socket and the glass specimen. The load is transmitted from the steel attachment with a pin to the steel socket, which is bolted to the reinforcement bars of the specimen. Regarding the boundary conditions, the attachment hinge to the testing machine is conceived frictionless so that there is no transfer of the bending moment. Hence, the specimen is subjected to a pair of self-equilibrating vertical forces, inducing symmetric internal forces in the adjoining sections. (see Fig. 5(b)). The distance from the point of the force application and the adjoining sections is denoted as a and it is equal to 550 mm for all the tests. Additionally, a lateral restraining system is built in steel and attached to the test setup. It is positioned in such a way to prevent lateral movements during the test, but to leave most of the specimen visible to the measurement system. As such, the kinematics can be captured by Digital Image Correlation (DIC) from one side and the crack pattern up to failure from the other.

With respect to the test procedure, the load is applied in displacement-controlled quasi-static regime until failure of the specimens. A universal testing machine Instron 5980 Series Dual Column Floor Frame with a capacity of 100 kN is used.

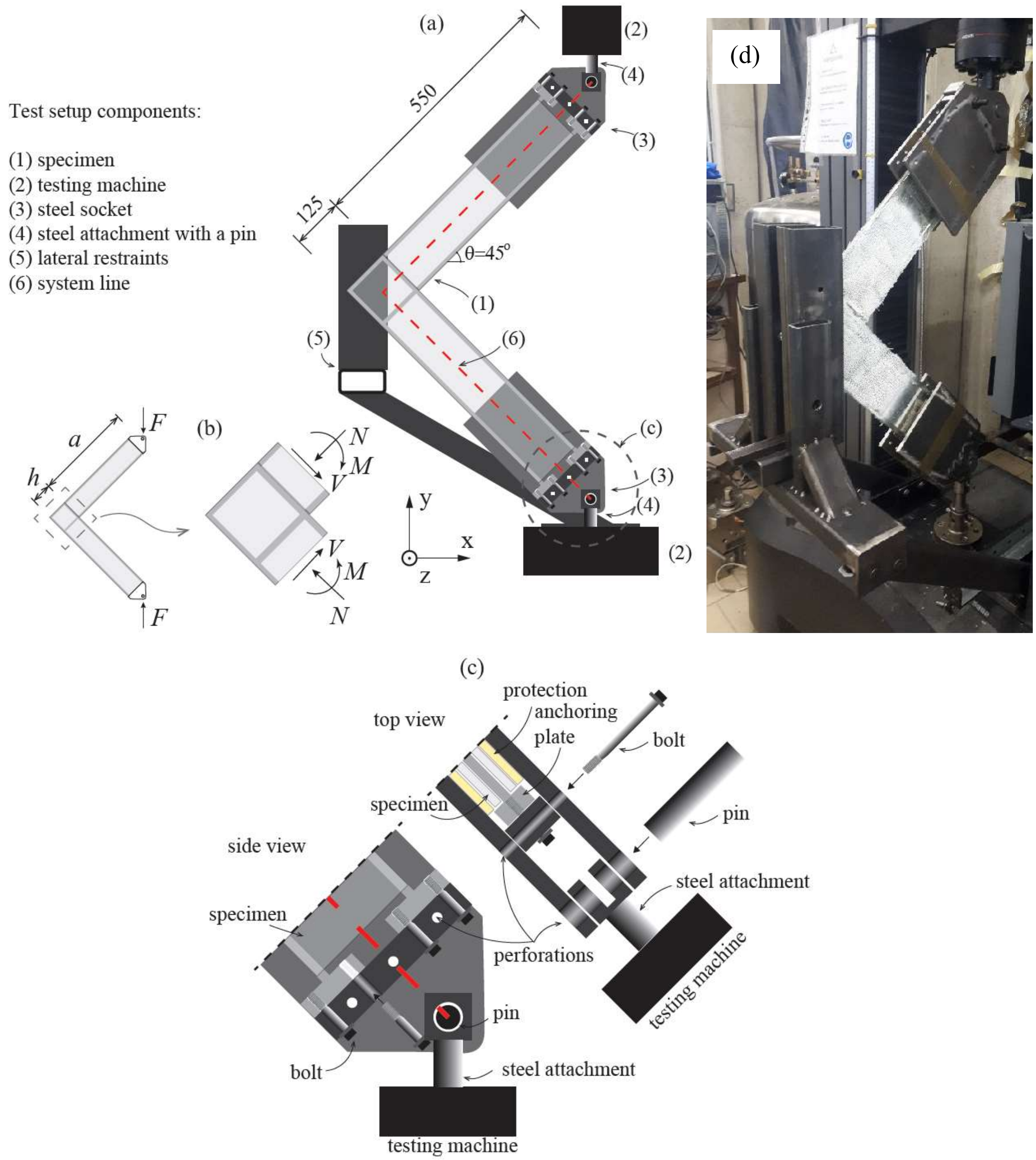

Fig. 5: (a) Schematic view of test setup and (b) transfer of forces in the test, (c) detail of the steel socket and (d) image of the setup.

2.3 Measurements

Measurements of the kinematics of the outer glass panes are performed by means of a DIC system. For that reason, a speckle pattern is applied on one side of the specimen, as illustrated in Fig. 6(a). The area covered encompasses the core and part of both adjoining elements so that the complete displacement field of the region of interest can be obtained. Another side of the specimen is left clean and at that location the crack pattern is recorded. Two digital cameras Prosilica GT3400, c-mount, 1-inch chip, GBit, 2704x3384@13 Hz (9 megapixel) are used. The size of the pixels was between 0.257 mm and 0.282 mm, whereas the size of the painted speckles on the surface was between 1 and 2 mm. The cameras' acquisition rate was set equal to 1 Hz for all the tests. The photos were post-processed using VIC3D software by Correlated Solutions [48]. Before beginning the experiments, photographs were taken with the displacement set to zero. The measured noise (the average between the maximum and minimum displacement values) was around 1/50 of a pixel for in-plane displacements and 1/30 of a pixel for out-of-plane displacements.

In addition, linear strain gauges are placed on the steel bar where there is an interruption of the outer glass panes and on the side of the continuous outer glass panes (see Fig. 6(b)). Strain gauges are oriented in such a way to measure axial deformation in the direction of the steel bars. The strain gauges with the designation CEA-06-125UN-120, manufactured by Micro-Measurements, were used.

As a result, deformations of both brittle and ductile components are tracked so that one can describe the post-fracture and the ultimate behaviour.

To calculate the relative rotation angle θ between the beam and the column components, displacements of two points from each side are tracked as depicted in Fig. 6(b). Points b_1, b_2, c_1 and c_2 correspond to the undeformed state while points b'_1, b'_2, c'_1 and c'_2 correspond to the deformed state of the joint for the beam and the column, respectively. The expressions for the angle calculation are given in Annex A.

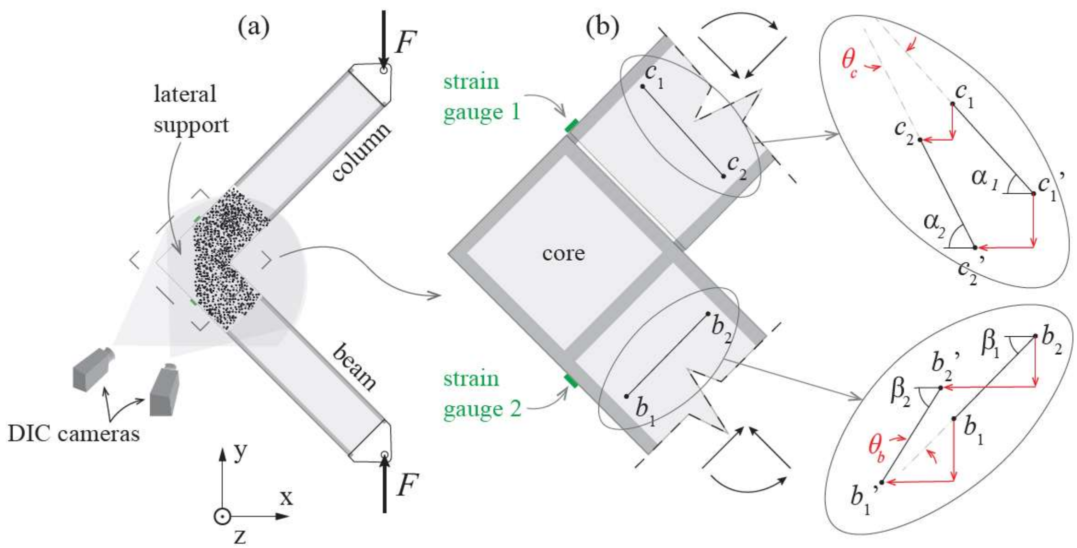

Fig. 6: Determination of the kinematics using DIC measurement system: (a) position of the strain gauges and speckle pattern, (b) calculation of the relative angle θ.

3. EXPERIMENTAL RESULTS

3.1 Rotational behaviour

Fig. 7 summarizes M - θ curves for SG- and UV-laminated specimens, separately. Also, an evolution of the tensile strains in the steel (ε_s), normalized by the yielding strain (ε_y), are plotted in the column-core cross-section (at this section the glass is fully interrupted) and the beam-core adjoining cross-section (continuous outer glass panes). Finally, the most characteristic crack patterns and failure modes are indicated next to the corresponding curves in Fig. 7. The latter are more elaborated in Fig. 8 and in Annex B for all the specimens.

From the experimental results three characteristic failure modes can be observed: (a) crushing failure (CF) of the joint core due to the brittle failure of glass in compression, (b) plastic failure (PF) of the adjoining sections due to yielding of the steel bars in tension and (c) failure due to debonding (DF) of one of the bars in tension. Finally, combined failure modes occurred in some of the tests.

Regarding the evolution of the tensile strains in the steel, it is worth noticing that the strains at the position of the column-core adjoining cross-section (where the glass is interrupted – strain measured with strain gauge 1) have systematically a higher value than those at the beam-core section (side of the continuous outer glass panes – strain measured with the strain gauge 2). This is due to the presence of the glass interruption in the pre-fracture phase. If the bond between steel and glass is able to engage a significant shear interaction, the strains are reduced to a large extent.

Crushing failure (CF) is characterized by brittle failure of a compression glass field in the joint core. It results in a sudden drop of the bending moment upon reaching its ultimate value with a sharp peak behaviour. Fig. 7(a) indicates that this type of failure occurred prior to the yielding of the reinforcement in case of SG1010. However, in case of SG0810 (see Fig. 7(b)) the crushing happened after yielding of the reinforcement (PF-CF). The yielding occurred mainly because of the lower and steel quality whereas the crushing of glass occurred due to the concentrated deformations in the core of the joint as it experienced significant plastic rotation. . This resulted in a lower value of the failure moment and a higher value of the ultimate rotation in case of SG0810.

Plastic failure (PF) occurs when the yielding stress in the steel is reached. After this moment strain hardening takes place. This behaviour can be observed in case of SG1005 and UV1005-1 since they possess a low reinforcement ratio (see Fig. 7(c) (f)). Specimen UV1005-2 experienced a debonding failure due to the formation of large bubbles at certain positions in the liquid resin before the curing process. The presence of bubbles reduced the bonding area and, consequently, the bond strength. While this did not affect the magnitude of the ultimate moment, which is comparable to the first specimen, it altered the failure mode from ductile plastic failure to debonding failure. Plastic failure normally occurs at the weakest section of the connection, which in this case is the fully interrupted section.

Debonding failure (DF) mode occurred for all the specimens produced with the UV curing technology, except the previously explained UV1005-1 (see Fig. 7(d) (e) (f)). This failure mode is developed when the tensile force in the steel is higher than the bonding strength of the interlayer. The failure due to debonding of a bar in tension results in a progressive loss of the load in the M - θ curve with a smooth peak behaviour.

In conclusion, the diversity of failure modes is a consequence of the differences in geometry of the configurations and mechanical and bonding properties of the interlayers used.

Fail-safe behaviour of such connections (governed by yielding of the reinforcement) is reached by a certain balance between glass panes thickness and amount of steel. However, the overall behaviour of such joints as well as the value of the plastic moment will depend on the steel-glass bonding surface available in the configuration.

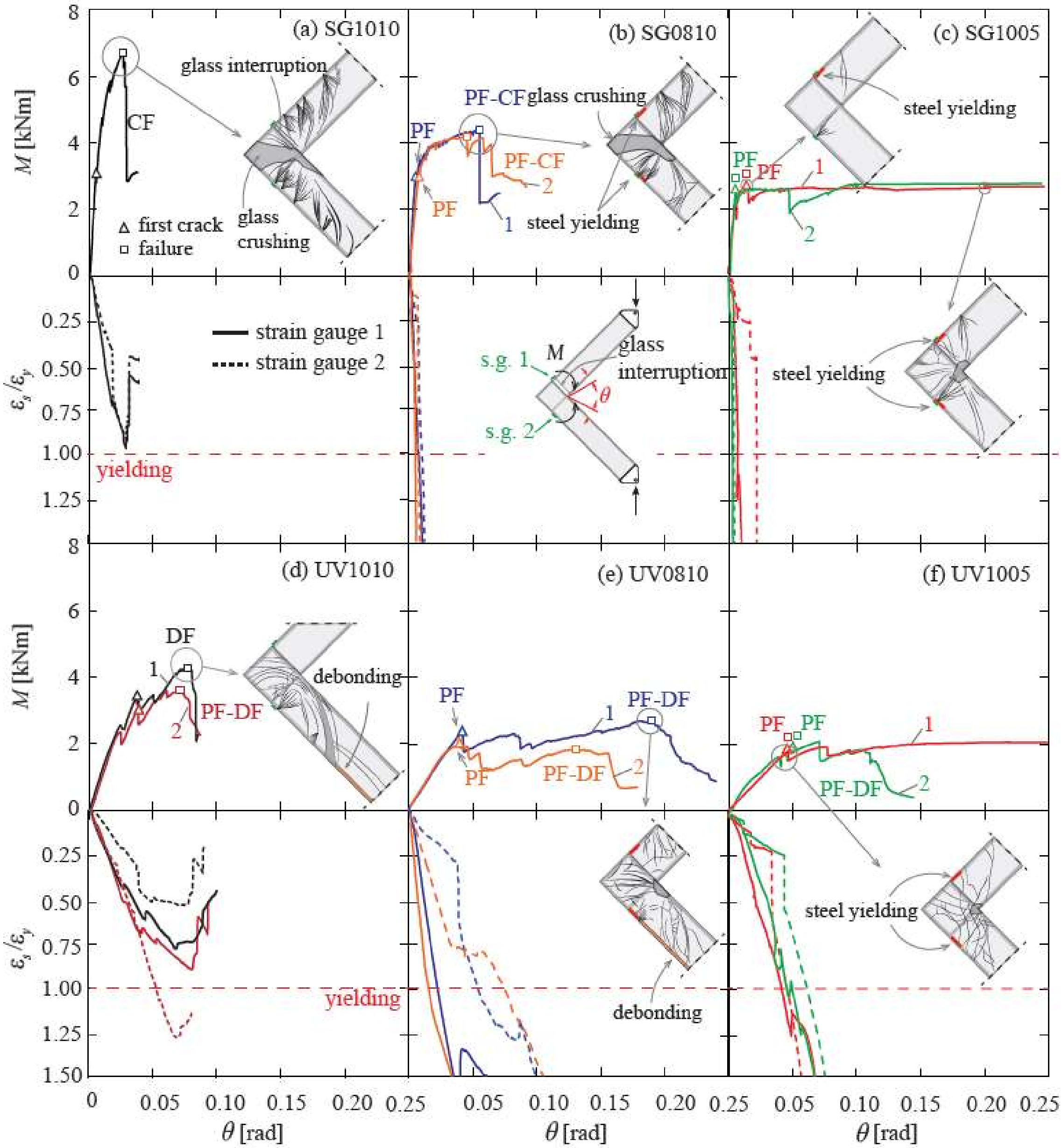

Fig. 7: M - θ curves, tensile strains evolution and typical failure modes (CF – crushing failure, PF – plastic failure and DF – debonding failure).

The crushing of the glass occurs when the applied compressive force in the cracked joint core reaches the compressive strength of the laminated glass. Larger thickness of the glass means a stronger joint core and a larger value of the crushing force. The crushing failure may occur before or after yielding of the tensile reinforcement, depending on the reinforcement ratio and its bond conditions. If the tensile reinforcement yields, it means that the applied moment exceeds the plastic capacity of the cross-section. The ultimate moment can reach larger values than the plastic moment due to the hardening of the steel. Larger reinforcement ratio yields larger values of the plastic capacity of the hybrid section. Finally, the debonding failure occurs when the stresses in the bonding areas between steel and glass achieve larger values than the bonding resistance. Debonding failure can be prevented if the larger bonding area is provided as well as an interlayer with stronger bond is used.

The most typical values related to the overall mechanical performance of the joints are summarized in Table 3. The main characteristics (bending moment M at the adjoining section, relative rotation θ and the strain states ε_{sg1} and ε_{sg2} in the steel bars) are reported at the moment of the first fracture (denoted with a subscript f) and at failure (denoted with a subscript u). The post-fracture capacity is quantified by means of the ratios between the values of the bending moments (M_u / M_f) and of the relative rotations (θ_u / θ_f) at failure ($_u$) and at first fracture ($_f$). These values are indicated in Fig. 7 by triangles (at first fracture) and squares (at failure).

In terms of the moment at first fracture, it is observed that the values for UV-laminated specimens are lower than in the case of SG-laminated specimens. The rotation at first fracture corresponds to the stiffness of the interlayer and bonding area, generally having larger values with a smaller bonding area and less stiff interlayer. UV-laminated specimens exhibit much larger rotations at first fracture. The cross-sections of the steel bars tested in this work differ, as well as the steel quality. However, the steel bars have the same modulus of elasticity. Therefore, the initial stiffness of the joints can be compared. Evidently, joints with larger reinforcement sections, bonding areas, and stiffer interlayers exhibit steeper initial slopes. Similar trends can be observed for the ultimate moment and rotation. These values depend on the stiffness, as well as on the strength of the components, as explained previously in this section. Regarding the measured tensile strains in the reinforcement, variability in the results is noticeable. Generally, tensile strains in the steel are larger at the interrupted section because the tensile force in this section is carried completely by the steel. In the beam, values are smaller since tension is carried by both steel and glass before the first crack. Strains are larger in the case of a smaller reinforcement ratio. Additionally, it can be observed that the difference in strains can be significant in the post-fracture domain (see, for example, SG1005-1 and SG1005-2). This is because the strain is measured locally by a strain gauge, and there might be some effects in the vicinity of the measurement location influencing the strains. These effects include cracking in the glass and local debonding of the interlayer. Local debonding of the SentryGlas® interlayer can occur prior to the first fracture, as is the case in SG1005-1.

Table 3: Overview of performance of the joints.

Name	Failure mode	M_f [kNm]	θ_f [rad]	$\varepsilon_{sg1,f}/\varepsilon_y$ ($\varepsilon_{sg2,f}/\varepsilon_y$)	M_u [kNm]	θ_u [rad]	$\varepsilon_{sg1,u}/\varepsilon_y$ ($\varepsilon_{sg2,u}/\varepsilon_y$)	M_u / M_f [-]	θ_u / θ_f [-]
SG1010	CF	3.32	0.004	0.22(0.15)	6.95	0.024	0.94(0.89)	2.09	5.16
SG0810-1	PF-CF	3.01	0.005	0.62(0.21)	4.38	0.057	>7.00(5.17)	1.45	9.92
SG0810-2	PF-CF	2.90	0.007	0.85(0.69)	4.20	0.046	5.64(3.90)	1.45	6.57
SG1005-1	PF	2.67	0.013	4.41(0.25)	2.67	0.014	4.41(0.25)	1.00	1.00
SG1005-2	PF	2.52	0.005	8.42(3.49)	2.52	0.005	8.50(3.57)	1.00	1.00
UV1010-1	DF	3.30	0.039	0.58(0.38)	4.16	0.076	0.76(0.55)	1.26	2.04
UV1010-2	PF-DF	3.18	0.038	0.53(0.58)	3.63	0.053	0.87(1.13)	1.15	1.42
UV0810-1	PF-DF	2.22	0.044	1.62(0.37)	2.52	0.185	4.76(3.47)	1.14	4.18
UV0810-2	PF-DF	2.02	0.035	1.60(0.81)	2.02	0.035	1.60(0.81)	1.00	1.00
UV1005-1	PF	1.78	0.047	1.14(2.13)	2.04	0.080	1.14(2.13)	1.15	1.67
UV1005-2	PF-DF	2.12	0.073	1.19(1.28)	2.12	0.079	1.19(1.28)	1.00	1.00

3.2 Crack patterns

Fig. 8 illustrates the most typical evolution and the influence of the interlayer on the crack patterns up to failure on an example of SG1010 and UV1010-1. The complete set of crack evolution patterns is provided in Annex B. The two specimens in Fig. 8 have the same cross-section but differ in their interlayers. It can be observed that the patterns are more symmetric with respect to the joint core in case of the SG-laminated specimen. The explanation lies in the SG interlayer's strong bonding performance.

This is related to the shear stiffness and bonding strength in the post-fracture domain. Finally, the specimens failed due to crushing of the glass in the core. In contrast, UV-laminated specimens have less regular crack patterns. This interlayer has a significantly lower stiffness with a possible pronounced local debonding in the surrounding of a formed crack. It can be observed that the first crack occurs at the critical section on the beam's side with the continuous outer glass panes. For the same reason the beam experiences more cracking. Cracks are less concentrated in the column due to the presence of the glass interruption in the external panes in the column-core adjoining section. Finally, the specimen failed due to debonding of the bar in tension.

Additionally, in the complete set of crack evolution patterns in Fig. 15 in Annex B, one can observe the influence of the area of the reinforcement, steel quality and steel-glass bonding area. Fig. 15 suggests that higher steel quality results in a more pronounced crack pattern at failure. The reason is that the higher tensile force will cause more cracks along the side of the beam/column in tension. This effect can be observed when comparing the crack pattern for SG1010 and SG0810. The additional effect of the smaller area of the reinforcement, steel quality and steel-glass bonding area can be seen in the case of SG1005, where the crack pattern is even less pronounced. Finally, the crack patterns of UV-laminated specimens appear to be more random without clear trends.

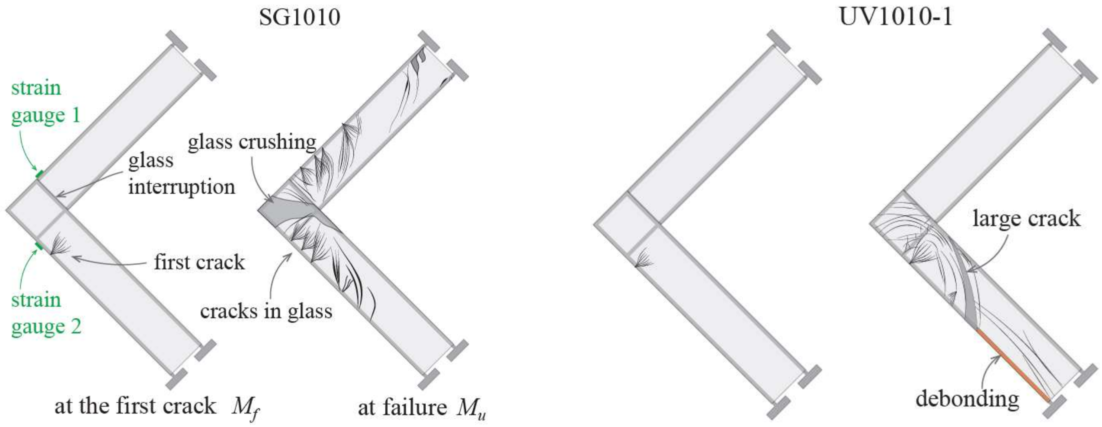

Fig. 8: Evolution of the crack patterns. Comparison between SG1010 and UV1010-1.

3.3 Effect of lamination technology

Fig. 9 illustrates the influence of the bonding technology on the rotational performance of the joints. The M - θ curves for the three different geometrical configurations are plotted in three separate graphs for the sake of comparison. The graphs clearly indicate the better performance of the SG-laminated specimens in all the three configurations. This holds for the initial stiffness, moment of the first fracture and the ultimate moment. Also, a change of the bonding technology resulted in a change of the failure mode. In particular, SG1010 failed due to glass crushing in the core, which is embodied in the sharp peak at failure, whereas UV1010 failed due to debonding, where a smoother peak behaviour is observed (see Fig. 9(a)). A similar observation could be made for SG0810 and UV0810 (see Fig. 9(b)). Finally, Fig. 9(c) indicates that the failure mode remains unaltered when SG1005 and UV1005 are compared. However, imperfections during the production process, such as the formation of large bubbles in the case of UV1005-2, can alter the failure mode from ductile plastic failure to debonding failure. In the case of UV1005-1, which failed in ductile plastic mode, a smaller value at the plateau is noticeable compared to SG1005. The reason is the lower stiffness of the interlayer. Generally, one can observe that the value of the ultimate moment is lower for the UV-laminates. However, UV-curable technology enables assembly on site. The lower performance of the joint built with this technology needs to be accounted for in design. This means a sufficient bonding surface needs to be provided to avoid debonding and an appropriate reinforcement ratio to achieve plastic failure.

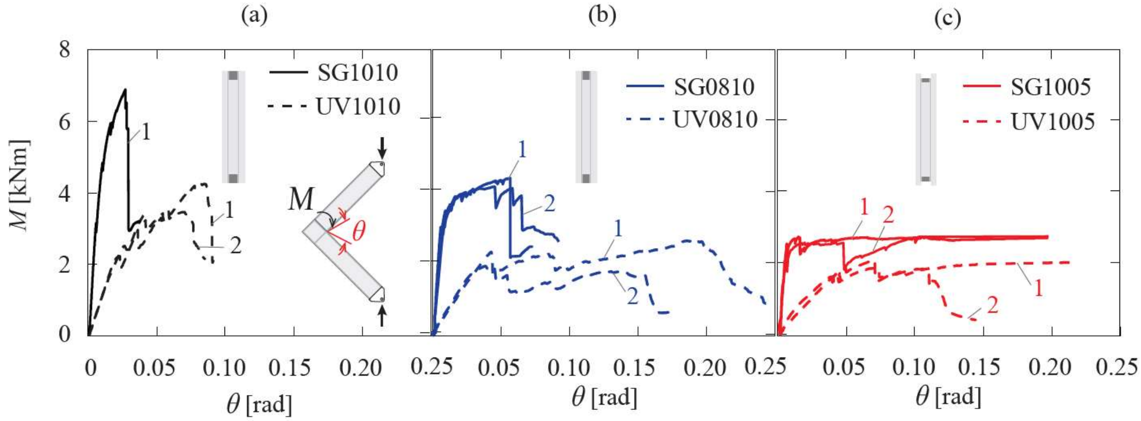

Fig. 9: Influence of the bonding technology on the rotational performance in case of: (a) SG(UV)1010, (b) SG(UV)0810 and (c) SG(UV)1005.

3.4 Principal strains in laminated glass

To illustrate the evolution of the principle strains in laminated glass with respect to the increasing load up to failure in SG-laminated and UV-laminated joints, this section analyses two specimens: SG1010 and UV1010-1. Counterplots depicting the principal tensile (ε_1) and compressive strains (ε_2) on the outer glass panes are plotted for SG1010 and UV1010-1 in Fig. 10 and Fig. 11, respectively. The direction of the vectors of the principal strains is indicated by black lines. The strains are reported for different load levels and at failure.

One can observe in Fig. 10 the first cracks (red colour) in the contour plot at 0.6 F_u in the beam of SG1010. Subsequently, these cracks propagate towards the compressed chord of the beam up to failure. It is evident that the direction of the principal tensile strains is perpendicular to the direction of the cracks. The principal compressive strains indicate that the most compressed zones are the inner sides of both the column and the beam (blue colour). Compression increases in these zones after the appearance of the first cracks for higher load levels. One can observe the principal compressive strain field in the core of SG1010 before the core crushes. The direction of these vectors is mostly along the diagonal of the core, whereas the values indicate a certain variability. The reason for this variability is the redistribution of stresses in the glass panes.

In the case of UV1010-1, as shown in Fig. 11, one can observe that the maximum principal tensile strains are more spread compared to SG1010. This is associated with the less stiff UV-curable interlayer, leading to a less controlled cracking process with a more random pattern of cracks. Ultimately, the specimen fails due to debonding, and a large crack appears in the beam.

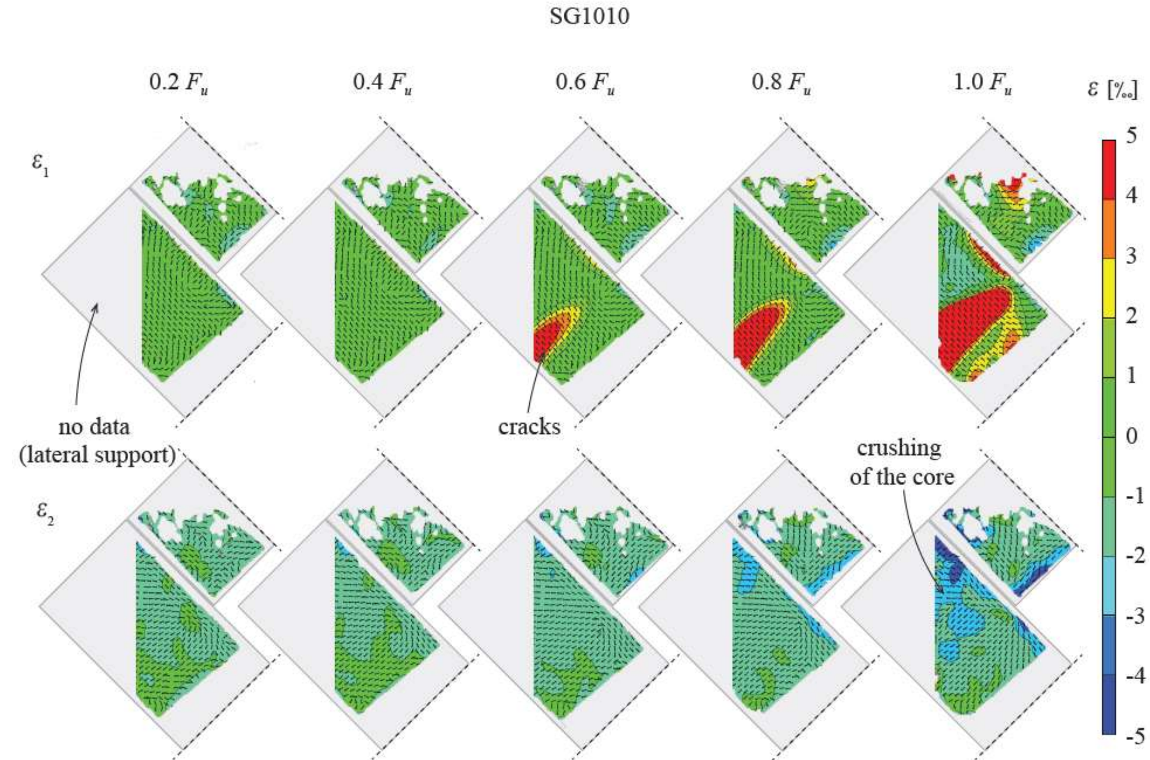

Fig. 10: Principal tensile strains (ε_1) and compressive strains (ε_2) in the outer panes of SG1010 specimen, where blue colour represents the largest compressive strains, red colour represents the largest tensile strains, and black lines indicate the direction of the principal strains.

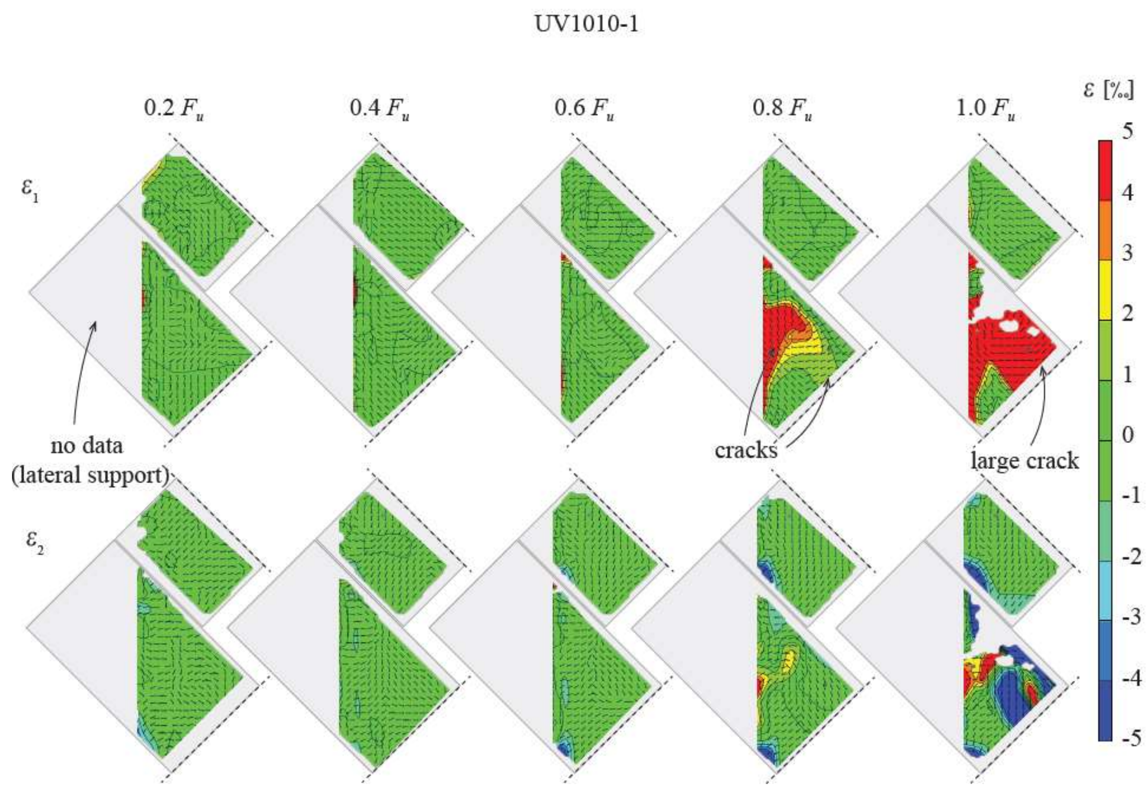

Fig. 11: Principal tensile strains (ε_1) and compressive strains (ε_2) in the outer panes of UV1010-1 specimen, where blue colour represents the largest compressive strains, red colour represents the largest tensile strains, and black lines indicate the direction of the principal strains.

3.5 Pull-out effect

Whenever there is a glass interruption in the hybrid components, the pull-out effect takes place. This can be in case of a crack in the post-fracture phase or at the location of intentionally interrupted glass. The latter is the case in the column-core adjoining section of the tested specimens. The opening causes a pull-out effect at the location of the tensile reinforcement. The cross-sections of the steel bars used in this work are different, as well as the steel quality. However, the steel bars have the same modulus of elasticity. In the linear-elastic domain, the pull-out effect depends on the steel-glass bonding area and the dimensions of the steel bar in tension. In the post-fracture domain, nonlinear pull-out behaviour occurs due to the cracking of the glass, plastic deformations in steel, and local debonding of the interlayer. It is worth mentioning that the pull-out measurements in this article focus only on the interrupted section, which is on the side of the column. This pull-out effect has influence on the rotational stiffness in both the linear-elastic and the post-fracture domain. In the beam with the continuous outer glass panes, the pull-out effect takes place only after the first cracks appear. The position of the first crack is random, hence the quantification of the pull-out effect is more complex.

Fig. 12(a) illustrates a deformation of the joint including the pull-out opening displacement (w). This quantity is defined as the relative displacement between the point in the joint core and the point on the side of the column. The force T_s is the pull-out stress in the axis of the tensile reinforcement. The force T_s is determined using Eq.(1):

$$T_s = \frac{M}{z} - \frac{N}{2} \tag{1}$$

where M and N are the experimental bending moment and normal force at the section of the glass interruption, respectively. The distance between the two reinforcement bars is denoted as z.

Fig. 12(b) presents $T_s - w$ curves. The results for SG- and UV-laminated specimens are presented separately. For SG-laminated specimens, it is noticeable that the pull-out curves initiate with the initial slope in the linear-elastic domain and subsequently exhibit nonlinear behaviour. This nonlinear behaviour can be attributed to the cracking of the glass, plastic deformations in the steel and local debonding of the interlayer. As expected, the SG-laminated specimens possess much smaller pull-out displacement values for the same load level compared to the case of the UV-laminated ones. Based on the observation during the test, the latter exhibit much larger shear deformation in the interlayer from both side of the column and side of the joint core. In contrast, SG-laminated joints exhibit shear deformation in the interlayer on the side of the column whereas very small deformation in the core. The initial pull-out slope for SG1010 is somewhat steeper than for SG0810. The reason is the larger steel bar section of SG1010 whereas the steel-glass bonding surface is similar for both configurations. The slope in case of SG1005 is lower, since both the bar section and the bonding surface are smaller. Similar trends can be observed for the UV-laminated group of specimens. However, they show poorer performance due to the more flexible interlayer.

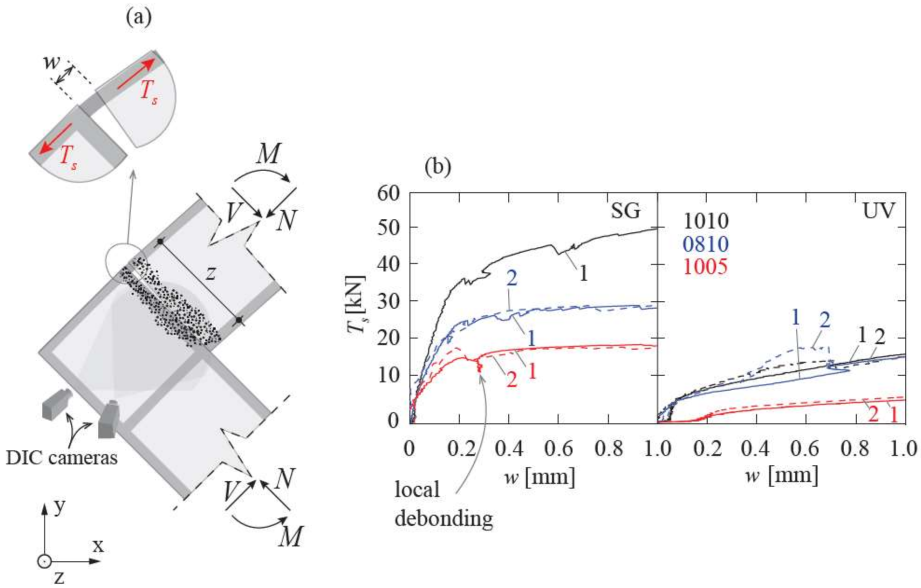

Fig. 12: (a) Pull-out opening displacement at the interrupted section and (b) $T_s - w$ curves.

Behaviour of the tensile reinforcement under the pull-out effect for SG0810-2 and SG1005-2 is presented in Fig. 13. The investigation of these two configurations is conducted to compare the effect of the different cross-section, dimensions of the steel section, and bonding area on the behaviour of the tensile reinforcement. Fig. 13(a) depicts the kinematics at the interrupted glass section. The kinematics are based on the $T_s - w$ curves. To measure the stress distribution in the tensile reinforcement two specimens SG0810-2 and SG1005-2 are equipped with strain gauges along the outer surface of the steel bar in tension (see Fig. 13(a)). The location of the strain gauges is defined by a local axis r. Fig. 13(b) presents the measured tensile stresses (σ_s) normalized by the yield stress of the steel. The stress is reported at a load step of 0.2 F_u. The behaviour up to 0.6 F_u belong to the linear-elastic domain whereas the curve for the load steps larger than 0.6 F_u belong to the post-fracture domain.

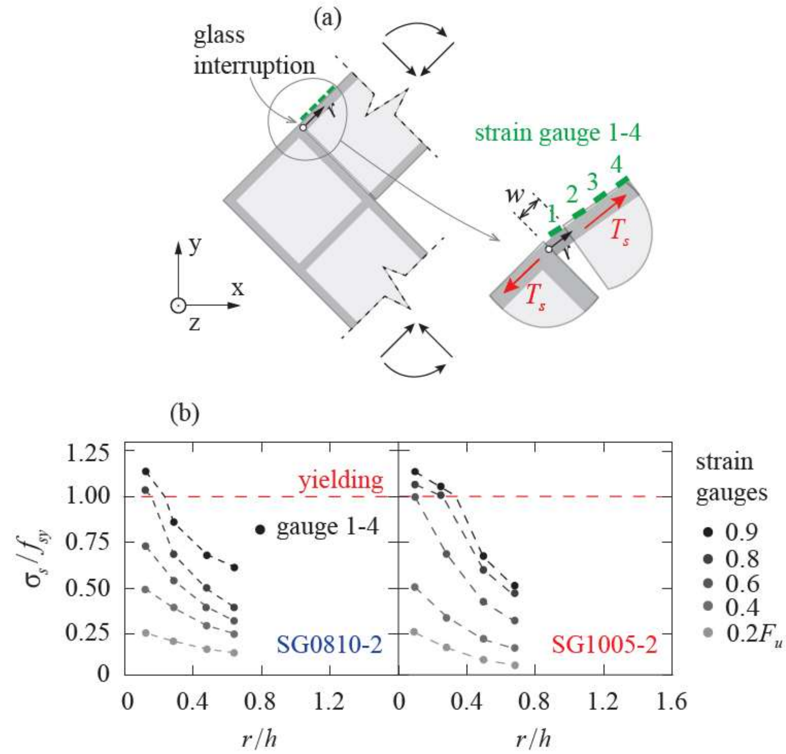

Fig. 13: (a) The location of the strain gauges to measure stresses along the reinforcement in tension. Measurement of strains in the steel bar in tension. (b) Stress on the outer surface of the steel bar in tension for SG0810-2 and SG1005-2.

It appears that the elastic stress distribution has a nonlinear decreasing trend. The reason is that the sectional behaviour transits between the fully interrupted to the fully hybrid one (as illustrated in Fig. 14(a)) due to the stress distribution along the adhesive interlayer.

The measured stresses are compared with the corresponding analytical stress predictions in Fig. 14(b). The analytical formulas are based on the hybrid section ($\sigma_{s,hyb.}$) and the fully interrupted section ($\sigma_{s,inter.}$) (see Fig. 14(a)). These stresses are calculated in the linear-elastic domain by Eq.(1) and Eq.(2), respectively.

$$\sigma_{s,inter.} = \frac{M}{I_s}\frac{h}{2} - \frac{N}{A_s} \tag{2}$$

$$\sigma_{s,hyb.} = \frac{M}{E_g I_{hyb.}}\frac{h}{2}E_s - \frac{N}{E_g A_{hyb.}}E_s \tag{3}$$

where A_s is the area of the reinforcement bar, $I_{hyb.}$ and $A_{hyb.}$ are second moment of inertia and area of the hybrid section, respectively.

It can be observed that the values of the measured stresses are in between the two stress predictions ($\sigma_{s,inter.}$ and $\sigma_{s,hyb.}$). The transition length, denoted as L_{trans}, is the length over which the actual stress distribution along the bar aligns with the analytical prediction for the fully hybrid section. It is noteworthy that, for the linear elastic domain (load levels up to $0.6F_u$), the transition length is on the order of magnitude of the height of the column (h), as extrapolated from the measurement data of both tested specimens. In the post-fracture domain (load levels higher than $0.6F_u$), the transition length appears to be somewhat larger. The increased length in the post-fracture domain is attributed to the presence of cracks that weaken the bonding properties, causing the section to behave as fully hybrid over a longer distance.

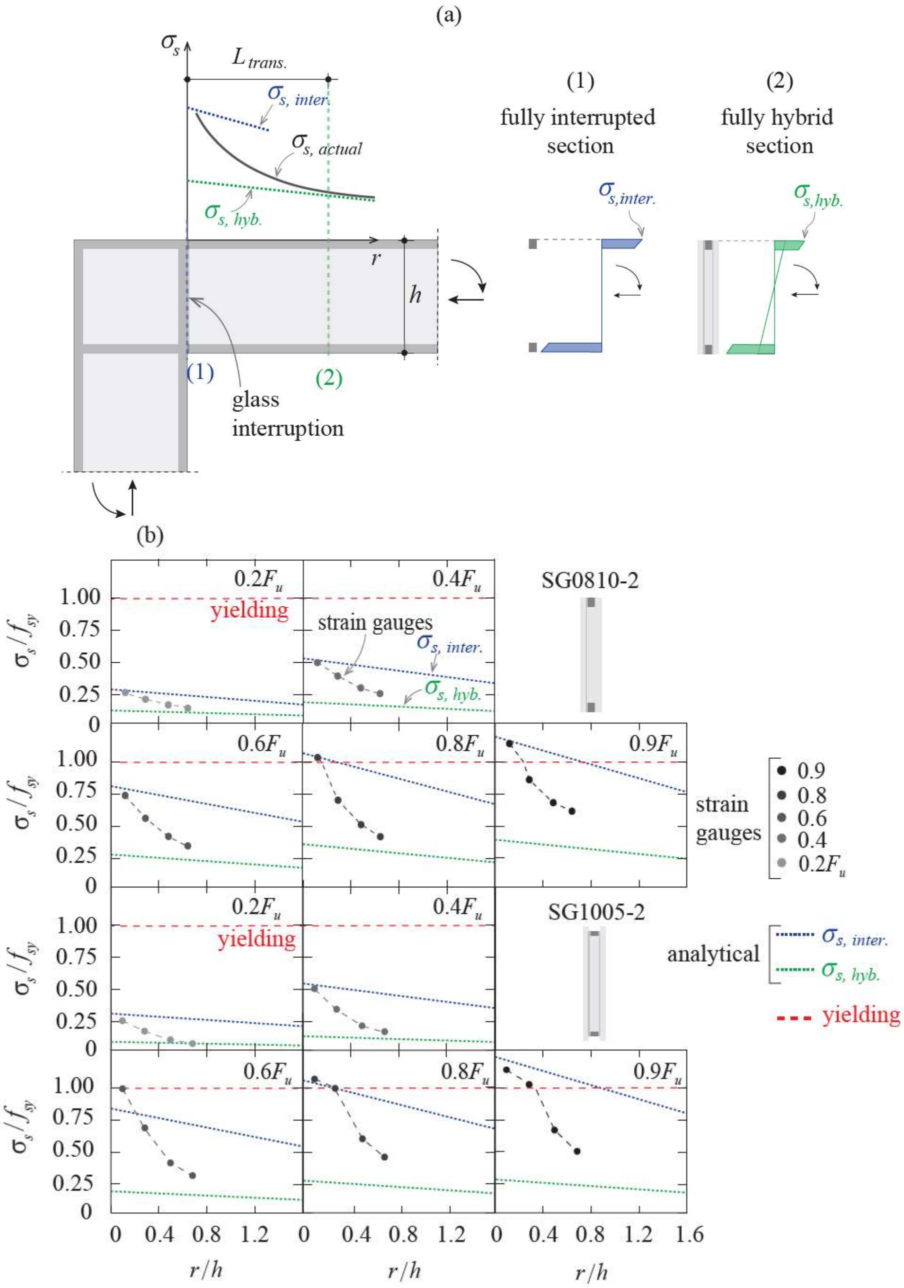

Fig. 14: Experimental stress along the reinforcement bar in tension for SG0810-2 and SG1005-2. Comparison with the analytical stress prediction in a hybrid section ($\sigma_{s,hyb.}$) and in a fully interrupted section ($\sigma_{s,inter.}$) for different load levels.

4. CONCLUSIONS

This paper outlines the process of production of a robust hybrid steel-glass joint prototype as well as its experimental testing and quantification of the influence of the main structural parameters. A joint prototype is built in several small-scale configurations and tested in a customized test setup. A common arrangement of setup elements for testing L-shaped joints is used. The setup consists of a combination of bolted and welded steel parts able to transfer horizontal and vertical forces from the jack to the joint inclined at 45°. The results are presented in terms of moment-rotation curves, strains evolution in the steel and the evolution of the crack patterns. A local bending effect is observed based on the stress measurements along the tensile reinforcement.

The hybrid laminated steel-glass joint prototype was tested in several small-scale configurations to assess the effect of the main structural parameters such as glass pane thickness, interlayer properties and reinforcement amount on its rotational characteristics. To explore the possibility of using different lamination technologies for the realization of joints in robust hybrid glass frames, two different bonding technologies are considered separately: (a) autoclave and (b) UV-curing lamination.

The main conclusions are the following:

1. It was found that the prototype is able to develop a significant post-fracture and rotational capacity in a properly balanced combination of structural and material parameters.
2. There are three possible failure modes: (a) brittle failure of the joint core due to crushing of the glass, (b) plastic failure of the adjoining sections due to yielding of the steel bars in tension and (c) failure due to debonding of one of the bars in tension. Combined failure modes occurred in some of the tests.
3. In case of the proposed connection, the interlayer stiffness has a crucial influence on the performance in the adjoining sections as well as in the core. Its stiffness largely determines the amount of energy stored in the glass and hence the evolution of the crack pattern and the final collapse behaviour. For instance, if the adhesive used does not possess sufficient shear stiffness, excessive slip of the reinforcement could lead to a reduced bearing capacity caused by a non-ductile failure mechanism rather than a plastic one.
4. The experiments suggest that a sufficiently strong steel-glass bond and core strength are necessary to provide a ductile failure of the joint. A higher reinforcement ratio and steel quality lead to brittle failure due to the crushing of the glass in the core. A higher interlayer stiffness is recommended to achieve a larger initial stiffness and a larger failure moment.
5. The findings indicate that the lamination technology could have a significant influence on the behaviour of the joints. SG-laminated joints evidently perform better regarding initial stiffness, fracture moment and the ultimate moment. The better performance can be attributed to the superior mechanical and bonding properties of the SG interlayer compared to the UV-curable resin.
6. However, UV-curable technology enables assembly on site. When this is a prerequisite, the lower performance of the joint built with this technology needs to be accounted for in the design. This means a sufficient bonding surface has to be provided to avoid debonding, as well as an appropriate reinforcement ratio to achieve plastic failure.
7. In the vicinity of a glass interruption a pull-out effect takes place. This effect is characterized by the opening displacement at the location of the bar in tension. Tensile stresses are measured along the reinforcement bar by means of strain gauges. It was observed that the sectional behaviour transits from a fully interrupted to a hybrid section over a certain transition length.
8. All the tested specimens are small-scale prototypes of the beam-column joint with identical dimensions. Therefore, drawing conclusions about size effects is not possible. It is recommended for future research to include joints of various sizes and different beam-column height ratios to explore potential size effects.

REFERENCES

[1] Veer F. A., Louter P.C., Bos F.P., and L. P. T. Schetters, “Reinforced segmented float glass, a novel way to create safe transparent beams,” Pôle VerrierColloque “Verre, matériau fonctionnel du futur”novembre 06, Nancy, 2006.

[2] K. Martens, R. Caspeele, and J. Belis, “Development of Reinforced and Posttensioned Glass Beams: Review of Experimental Research,” *Journal of Structural Engineering*, vol. 142, no. 5, p. 04015173, May 2016, doi: 10.1061/(asce)st.1943-541x.0001453.

[3] C. Louter, “Adhesively bonded reinforced glass beams,” 2007. [Online]. Available: www.glass.bk.tudelft.nl

[4] P. Christiaan. Louter, *Fragile yet Ductile : structural aspects of reinforced glass beams.* [s.n.], 2011.

[5] K. Martens, R. Caspeele, and J. Belis, “Membrane action in reinforced glass beam systems: Experimental setup and results,” *Constr Build Mater*, vol. 192, pp. 301–316, Dec. 2018, doi: 10.1016/j.conbuildmat.2018.10.120.

[6] D. Delincé, D. Callewaert, J. Belis, and R. Van Impe, “Post-breakage behaviour of laminated glass in structural applications,” 2008. [Online]. Available: www.LMO.UGent.be

[7] F. P. Bos, “Stellingen behorend bij het proefschrift: Safety Concepts in Structural Glass Engineering-Towards an Integrated Approach,” 2009.

[8] C. Bedon and M. Santarsiero, “Transparency in Structural Glass Systems Via Mechanical, Adhesive, and Laminated Connections - Existing Research and Developments,” *Advanced Engineering Materials*, vol. 20, no. 5. Wiley-VCH Verlag, May 01, 2018. doi: 10.1002/adem.201700815.

[9] M. Overend, Q. Jin, and J. Watson, “The selection and performance of adhesives for a steelglass connection,” *Int J Adhes Adhes*, vol. 31, no. 7, pp. 587–597, Oct. 2011, doi: 10.1016/j.ijadhadh.2011.06.001.

[10] K. Machalická and M. Eliášová, “Adhesive joints in glass structures: effects of various materials in the connection, thickness of the adhesive layer, and ageing,” *Int J Adhes Adhes*, vol. 72, pp. 10–22, Jan. 2017, doi: 10.1016/j.ijadhadh.2016.09.007.

[11] C. Bedon and M. Santarsiero, “Transparency in Structural Glass Systems Via Mechanical, Adhesive, and Laminated Connections - Existing Research and Developments,” *Advanced Engineering Materials*, vol. 20, no. 5. Wiley-VCH Verlag, May 01, 2018. doi: 10.1002/adem.201700815.

[12] C. Bedon and M. Santarsiero, “Laminated glass beams with thick embedded connections – Numerical analysis of full-scale specimens during cracking regime,” *Compos Struct*, vol. 195, pp. 308–324, Jul. 2018, doi: 10.1016/j.compstruct.2018.04.083.

[13] M. Santarsiero, C. Louter, and A. Nussbaumer, “Laminated connections for structural glass components: a full-scale experimental study,” *Glass Structures and Engineering*, vol. 2, no. 1, pp. 79–101, Jun. 2017, doi: 10.1007/s40940-016-0033-2.

[14] M. Santarsiero, C. Bedon, and C. Louter, “Experimental and numerical analysis of thick embedded laminated glass connections,” *Compos Struct*, vol. 188, pp. 242–256, Mar. 2018, doi: 10.1016/j.compstruct.2018.01.002.

[15] C. Zhao, J. Yang, X.-E. Wang, and I. Azim, “Experimental and Numerical Investigation Into the Mechanical Behavior of Embedded Laminated Connections”, doi: 10.7480/cgc.7.4551.

[16] J. Denonville, K. Puller, W. Haase, and W. Sobek, “Langzeittragverhalten von in Verbundglas integrierten Lasteinleitungselementen,” *Stahlbau*, vol. 82, no. SUPPL. 1, pp. 117–127, Apr. 2013, doi: 10.1002/stab.201390057.

[17] S. Marinitsch, C. Schranz, and M. Teich, "Folded plate structures made of glass laminates: a proposal for the structural assessment," *Glass Structures and Engineering*, vol. 1, no. 2, pp. 451–460, Oct. 2016, doi: 10.1007/s40940-015-0002-1.

[18] T. Fildhuth, P. Joos, T. Wüest, M. Haller, and W. Stevels, "Development and behavior of a thin fitting connection for lamination with structural PVB," *Glass Structures and Engineering*, vol. 7, no. 3, pp. 415–439, Oct. 2022, doi: 10.1007/s40940-022-00198-6.

[19] P. Carvalho, P. J. S. Cruz, and F. Veer, "Connecting through reinforcement - Experimental analysis of a glass connection using perforated steel plates," in *Challenging Glass 3: Conference on Architectural and Structural Applications of Glass, CGC 2012*, IOS Press, 2012, pp. 187–194. doi: 10.3233/978-1-61499-061-1-187.

[20] K. Puller and W. Sobek, "Load-carrying behaviour of metal inserts embedded in laminated glass," in *Challenging Glass 3: Conference on Architectural and Structural Applications of Glass, CGC 2012*, IOS Press, 2012, pp. 307–314. doi: 10.3233/978-1-61499-061-1-307.

[21] C. Louter and M. Santarsiero, "Metal-to-glass bond strength of structural PVB," *Glass Performance Days*, vol. 2019, pp. 49–55, 2019.

[22] J. Torres, N. Guitart, and C. Teixidor, "Glass fins with embedded titanium inserts for the façades of the new Medical School of Montpellier," *Glass Structures and Engineering*, vol. 2, no. 2, pp. 201–219, Oct. 2017, doi: 10.1007/s40940-017-0049-2.

[23] P. Willareth and D. Meyer, "A new folding glass roof for the historic city swimming hall Zürich," *Glass Performance Days*, pp. 17–20, 2011.

[24] C. Louter, J. Belis, F. Veer, and J. P. Lebet, "Durability of SG-laminated reinforced glass beams: Effects of temperature, thermal cycling, humidity and load-duration," *Constr Build Mater*, vol. 27, no. 1, pp. 280–292, Feb. 2012, doi: 10.1016/j.conbuildmat.2011.07.046.

[25] K. Machalická and M. Eliášová, "Adhesive joints in glass structures: effects of various materials in the connection, thickness of the adhesive layer, and ageing," *Int J Adhes Adhes*, vol. 72, pp. 10–22, Jan. 2017, doi: 10.1016/j.ijadhadh.2016.09.007.

[26] J. Vervloed, A. Kwakernaak, and H. Poulis, "The Influences of Overlap Length, Bond Line Thickness and Pretreatmant on the Mechanical Properties of Adhesives: Focussing on Bonding Glass."

[27] V. A. Silvestru, M. Drass, O. Englhardt, and J. Schneider, "Performance of a structural acrylic adhesive for linear glass-metal connections under shear and tensile loading," *Int J Adhes Adhes*, vol. 85, pp. 322–336, Oct. 2018, doi: 10.1016/j.ijadhadh.2018.07.006.

[28] E. Cagnacci, M. Orlando, L. Salvatori, and P. Spinelli, "Four-point bending tests on laminated glass beams reinforced with FRP bars adhesively bonded to the glass," *Glass Structures and Engineering*, vol. 6, no. 2, pp. 211–232, Jun. 2021, doi: 10.1007/s40940-021-00147-9.

[29] J. Belis, D. Callewaert, D. Delincé, and R. Van Impe, "Experimental failure investigation of a hybrid glass/steel beam," *Eng Fail Anal*, vol. 16, no. 4, pp. 1163–1173, Jun. 2009, doi: 10.1016/j.engfailanal.2008.07.011.

[30] AH. Snijder, FA. Veer, R. Nijsse, G. Baardolf, and T. Romein, "Designing and testing an eight meter span glass portal frame," Darmstadt: In J. Schneider, & B. Weller (Eds.), Proceedings of the international conference at glasstec, 2014.

[31] W.-Y. Huang, "Master thesis: L-shaped Connection for Glass Portal Frame Structural analysis and its application," 2017.

[32] B. Weller, F. Nicklisch, V. Prautzsch, F. Döbbel, and S. Rücker, "Challenging Glass 2-Conference on Architectural and Structural Applications of Glass," 2010. [Online]. Available: www.bauko.bau.tu-dresden.de

[33] V. Prautzsch and B. Weller, "Untersuchung des Tragverhaltens geklebter Glas-Rahmenecken im Zeitstandversuch. Glasbau 2016. 1. Auflage. Herausgegeben von Bernhard Weller, Silke Tasche. 2016 Ernst & Sohn GmbH & Co. KG. Published 2016 by Ernst & Sohn GmbH & Co. KG.," 2016.

[34] M. Pejatovic, R. Caspeele, and J. Belis, "Numerical study of post-fracture behavior of a two-sided reinforced laminated glass beam-column connection prototype," *Glass Structures & Engineering*, Aug. 2022, doi: 10.1007/s40940-022-00193-x.

[35] K. Martens, R. Caspeele, and J. Belis, "Load-carrying behaviour of interrupted statically indeterminate reinforced laminated glass beams," *Glass Structures and Engineering*, vol. 1, no. 1, pp. 81–94, Jun. 2016, doi: 10.1007/s40940-016-0017-2.

[36] N. Wang, F. Zhou, Z. Li, Z. Xu, and H. Xu, "Experimental and numerical investigation on the L-joint composed of steel-plate composite (SC) walls under seismic loading," *Eng Struct*, vol. 227, Jan. 2021, doi: 10.1016/j.engstruct.2020.111360.

[37] N. Wang, F. Zhou, Z. Li, Z. Xu, and H. Xu, "Behavior of L-joint composed of steel-plate composite wall and reinforced concrete wall," *J Constr Steel Res*, vol. 176, Jan. 2021, doi: 10.1016/j.jcsr.2020.106439.

[38] J. Seo and A. H. Varma, "Behavior and design of steel-plate composite wall-to-wall corner or L-joints," *Nuclear Engineering and Design*, vol. 323, pp. 317–328, Nov. 2017, doi: 10.1016/j.nucengdes.2017.04.008.

[39] J. Seo, A. H. Varma, K. Sener, and D. Ayhan, "Steel-plate composite (SC) walls: In-plane shear behavior, database, and design," *J Constr Steel Res*, vol. 119, pp. 202–215, Mar. 2016, doi: 10.1016/j.jcsr.2015.12.013.

[40] K. Martens, "Statically Indeterminate Reinforced Glass Beams," Ghent, 2018.

[41] E. Volakos, C. Davis, M. Teich, P. Lenk, and M. Overend, "Structural performance of a novel liquid-laminated embedded connection for glass," *Glass Structures and Engineering*, vol. 6, no. 4, pp. 487–510, Dec. 2021, doi: 10.1007/s40940-021-00162-w.

[42] E. Volakos, C. Davis, M. Teich, P. Lenk, and M. Overend, "Temperature effects on the behaviour of liquid-laminated embedded glass connections," *Eng Struct*, vol. 274, Jan. 2023, doi: 10.1016/j.engstruct.2022.115164.

[43] D. Callewaert, J. Belis, D. Delincé, and R. Van Impe, "Experimental stiffness characterisation of glass/ionomer laminates for structural applications," *Construction and Building Materials*, vol. 37. pp. 685–692, Dec. 2012. doi: 10.1016/j.conbuildmat.2012.07.035.

[44] Allnex, "Technical Data Sheet Uvekol S15," 2019.

[45] K. Martens, "Hyperstatische gewapende glazen liggers Statically Indeterminate Reinforced Glass Beams," 2017.

[46] "CEN 13474 Glass in building—Design of glass panes. 2 Design for uniformly distributed loads".

[47] B. Van Lancker, "PhD thesis: Experimental and Numerical Investigation of Two-Sided Bonded Glass-Steel Façade Units," 2021.

[48] Correlated Solutions, “Vic-3D 2010, Reference Manual,” 2010.

ANNEX A

Displacement of points used for the calculation of the relative rotations are depicted in Fig. 6(b). The contribution to the relative rotation of the column is calculated by using formulas (1) - (3):

$$\alpha_1 = atan\left(\frac{Y_{c_1} - Y_{c_2}}{X_{c_2} - X_{c_1}}\right) \tag{1}$$

$$\alpha_2 = atan\left(\frac{Y'_c}{X'_c}\right) = atan\left(\frac{Y_{c_1} - Y_{c_2} + v_{c_2} - v_{c_1}}{X_{c_2} - X_{c_1} + u_{c_1} - u_{c_2}}\right) \tag{2}$$

$$\theta_c = \alpha_2 - \alpha_1 \tag{3}$$

The contribution to the relative rotation of the beam is calculated by using formulas (4) - (6):

$$\beta_1 = atan\left(\frac{Y_{b_2} - Y_{b_1}}{X_{b_2} - X_{b_1}}\right) \tag{4}$$

$$\beta_2 = atan\left(\frac{Y'_b}{X'_b}\right) = atan\left(\frac{Y_{b_2} - Y_{b_1} + v_{b_1} - v_{b_2}}{X_{b_2} - X_{b_1} + u_{b_1} - u_{b_2}}\right) \tag{5}$$

$$\theta_b = \beta_2 - \beta_1 \tag{6}$$

The total relative rotation is a sum of the two contributions.

$$\theta = \theta_c + \theta_b \tag{7}$$

ANNEX B

Fig. 15 presents the crack pattern at the moment of the first crack and at failure all the samples.

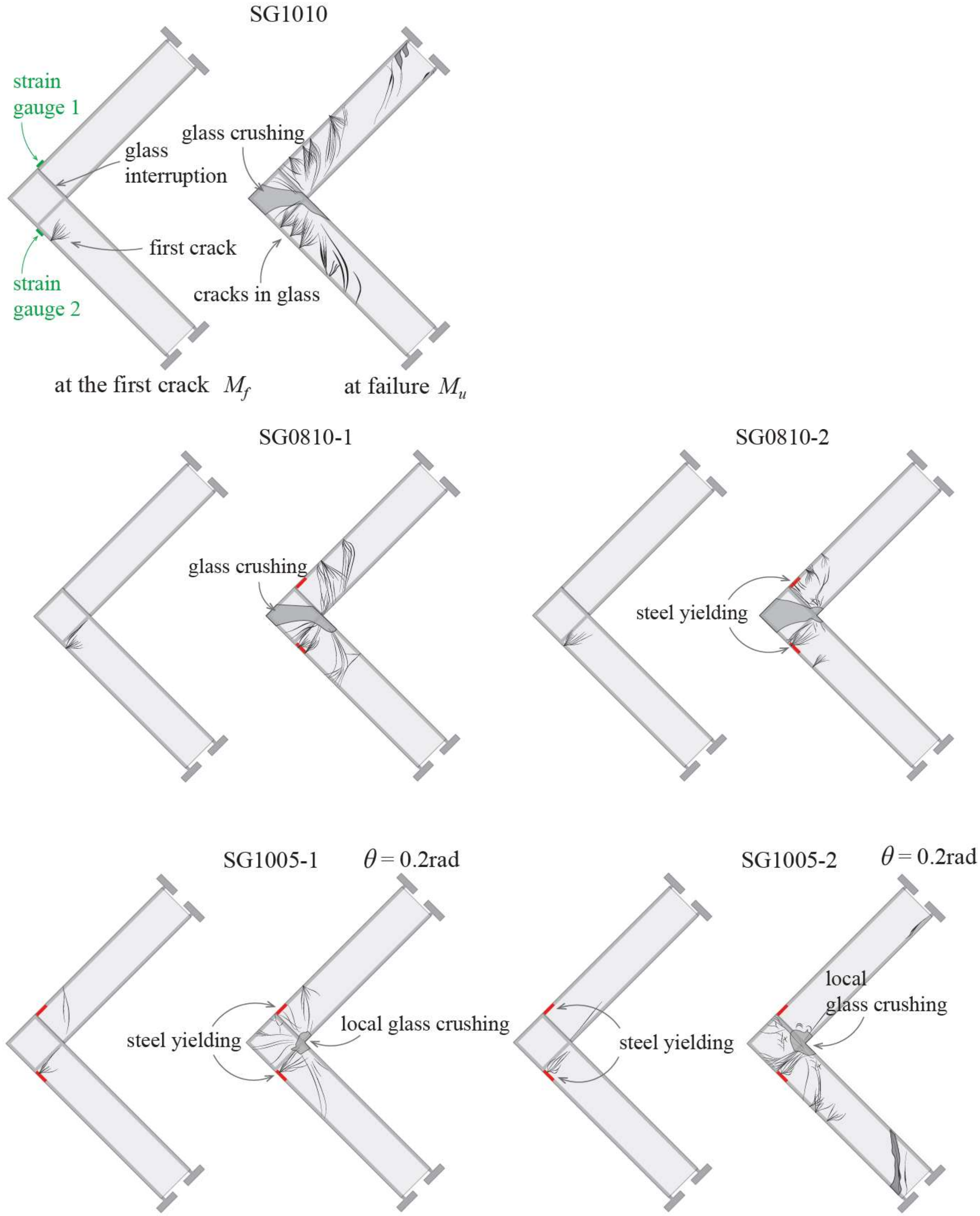
SG1010
strain gauge 1
glass interruption
glass crushing
first crack
strain gauge 2
cracks in glass
at the first crack M_f
at failure M_u
SG0810-1
glass crushing
SG0810-2
steel yielding
SG1005-1
$\theta = 0.2$rad
steel yielding
local glass crushing
SG1005-2
$\theta = 0.2$rad
steel yielding
local glass crushing

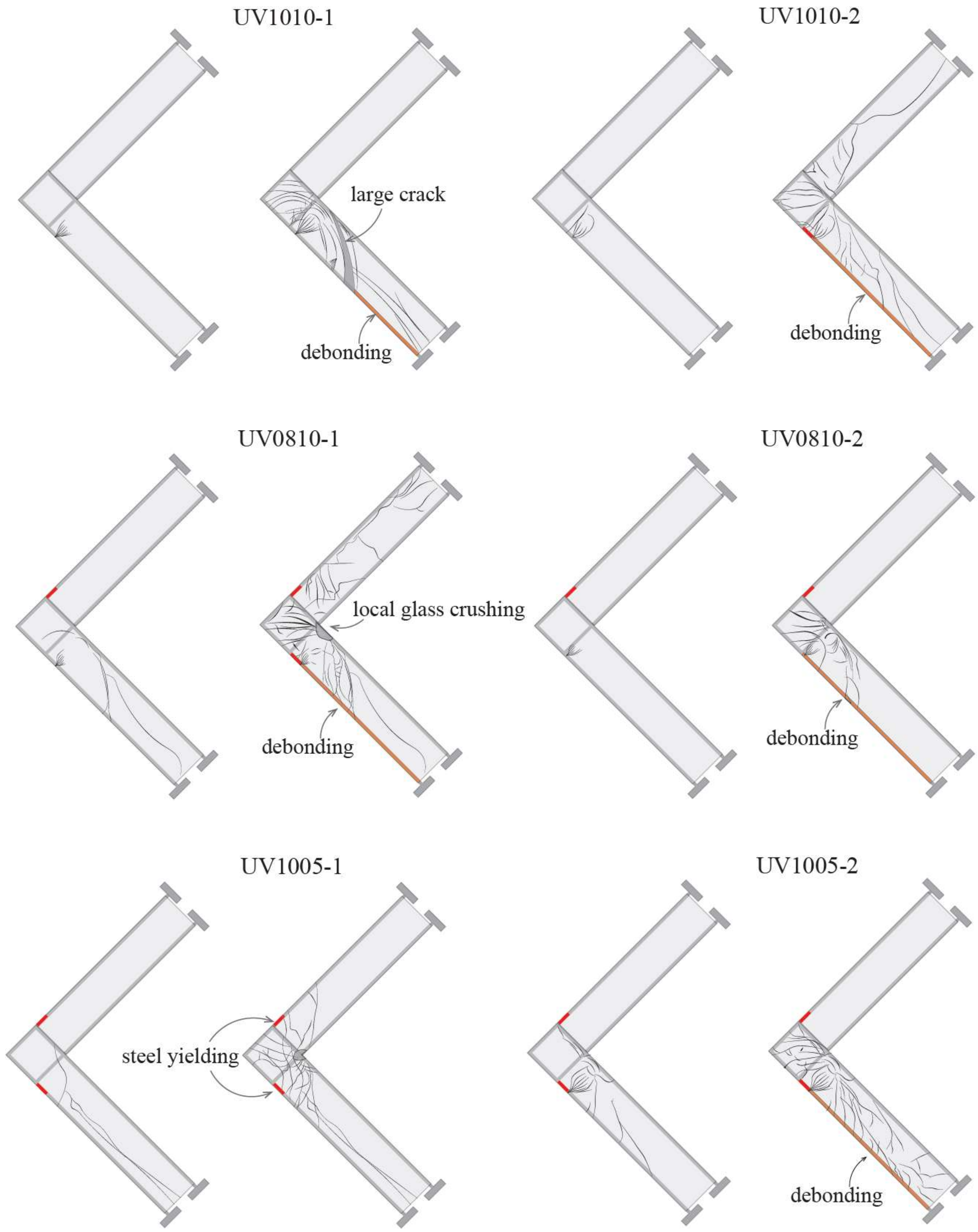

Fig. 15: Evolution of the crack patterns.